J Electroceram (2008) 20:159–165
DOI 10.1007/s10832-007-9128-0

Constitutive modelling of rate-dependent domain switching effects in ferroelectric and ferroelastic materials

A. Arockiarajan · A. Menzel · W. Seemann

Received: 29 November 2006 / Accepted: 9 April 2007 / Published online: 22 May 2007

Abstract In this contribution, a micro-mechanically motivated constitutive model for rate-dependent domain switching effects is studied. The main focus consists in the development of a three-dimensional finite element framework capturing phase-transformations, whereby for the sake of simplicity each finite element will represent one individual grain. For the investigation of phase-transitions, the onset of so-called domain switching processes is initiated by means of an energy-based criterion. During such switching processes, nucleation and propagation of domain wall motion is incorporated via a straightforward volume fraction concept combined with a simple linear kinetics theory. Moreover, grain boundary effects are accounted for, whereby a macro-mechanically motivated probabilistic approach has been chosen. Based on the proposed formulation, representative simulations are elaborated which provide further insight into the highly nonlinear behaviour of ferroelectric and ferroelastic materials.

A. Arockiarajan
Department of Applied Mechanics,
Indian Institute of Technology Madras, Chennai, India

A. Menzel (✉)
Department of Mechanical Engineering,
Institute of Mechanics and Control Engineering,
Chair of Continuum Mechanics, University of Siegen,
Paul-Bonatz-Str. 9-11, D-57076 Siegen, Germany
e-mail: menzel@imr.mb.uni-siegen.de
URL: http://www.uni-siegen.de/fb11/km

W. Seemann
Department of Mechanical Engineering,
Institute for Engineering Mechanics,
University of Karlsruhe, Karlsruhe, Germany

Keywords Ferroelectricity · Ferroelasticity · Rate-dependency · Volume fraction concept · Finite element method · Grain boundary effects

1 Introduction

Smart materials are nowadays frequently used in modern structural design and automatically perform according to specific sought functions under various loading scenarios without prior intervention by the 'users'. To give an example, ferroelectric materials have attracted considerable interest and are widely used for automotive, medical and microelectronic applications; see for instance Jaffe et al. [1]. These materials exhibit almost linear response as long as small electromechanical loads act on them. If the applied loads are sufficiently large, however, severely nonlinear response is observed. The main reason for this behaviour is identified as the change in so-called spontaneous polarisation directions as well as distortion of the underlying unit-cells which renders changes in the strain-state, namely spontaneous strains.

Modelling approaches developed for the simulation of nonlinear ferroelectric/ferroelastic behaviour can be classified into two major categories: on the one hand, phenomenological or macro-mechanical formulations as based on a certain set of state variables, which are incorporated into those functions of interest, have been proposed. Constitutive relations and related evolution equations can then be established by means of thermodynamic considerations; see the contributions by Lynch and McMeeking [2], Kamlah and Tsakmakis [3], Landis [4], or Schröder and Gross [5] among others. On the other hand, micro-mechanical approaches have been

investigated as based on direct physical insights of the material. Apparently, different length scales—related to the particular microstructural aspect of interest—can be addressed when setting up such theories. The subsequently studied model accounts for the bulk material consisting of several grains which are initially oriented by random. To analyse the macroscopic response, use of standard volume averaging techniques will be made; in this regard, the reader is also referred to the works by Lu et al. [6], Chen et al. [7], and Hwang et al. [8].

Concerning numerical investigations, finite element techniques can efficiently be used for the simulation of piezoelectric materials and thereby serve for both, micro-mechanical approaches as well as for phenomenological modelling concepts. Fundamental derivations for the problem at hand as based on a variational scheme are discussed in Allik and Hughes [9]. Later on, nonlinear coupled finite element formulations for piezoelectric continua have been proposed, for instance, by Gaudenzi and Bathe [10]; see also the contributions by Hwang and Waser [11], Schröder and Gross [5], or—in view of the subsequently applied algorithmic framework—Arockiarajan et al. [12] for further details on the numerical treatment.

The paper is organised as follows: Section 2 reviews essential balance relations and constitutive equations. The switching criterion applied for the initiation of domain wall motion as well as the adopted volume fraction concept and the probabilistic approach to capture intergranular effects are addressed in Section 3. Numerical examples based on the highlighted model are discussed in Section 4. Finally, the paper is closed with a short summary in Section 5.

2 Constitutive model

Piezoelectric materials exhibit strongly temperature-dependent behaviour. Accordingly, the materials of interest posses cubic symmetry for operating temperatures above the so-called Curie temperature. Phase-transformations, however, occur for operating temperatures below this Curie temperature so that the underlying unit-cells switch to tetragonal or rhombohedral structures. In the following we briefly review balance and constitutive equations essential to model these effects within a continuum approach.

Consider a continuum body of interest denoted by B with configuration $\mathcal{B} \subset \mathbb{R}^3$ as characterised by placements $\boldsymbol{x} \in \mathbb{R}^3$. As this work proceeds, the displacement field $\boldsymbol{u} \in \mathbb{R}^3$ together with the electric potential $\phi \in \mathbb{R}$ constitute the essential degrees of freedom so that essential balance relations are represented by the balance of linear momentum and Gauß' law, namely

$$\begin{aligned} \boldsymbol{0} &= \nabla \cdot \boldsymbol{\sigma} + \boldsymbol{b} && \text{in} \quad \mathcal{B} \\ \boldsymbol{u} &= \boldsymbol{u}^p && \text{on} \quad \partial\mathcal{B}_u \\ \boldsymbol{t} &= \boldsymbol{t}^p = \boldsymbol{\sigma} \cdot \boldsymbol{n}_\sigma && \text{on} \quad \partial\mathcal{B}_\sigma \end{aligned} \tag{1}$$

$$\begin{aligned} 0 &= \nabla \cdot \boldsymbol{D} - \rho_f && \text{in} \quad \mathcal{B} \\ \phi &= \phi^p && \text{on} \quad \partial\mathcal{B}_\phi \\ -q &= -q^p = \boldsymbol{D} \cdot \boldsymbol{n}_D && \text{on} \quad \partial\mathcal{B}_D \end{aligned} \tag{2}$$

with $\partial\mathcal{B}_u \cup \partial\mathcal{B}_\sigma = \partial\mathcal{B}_\phi \cup \partial\mathcal{B}_D = \partial\mathcal{B}$ and $\partial\mathcal{B}_u \cap \partial\mathcal{B}_\sigma = \partial\mathcal{B}_\phi \cap \partial\mathcal{B}_D = \emptyset$. Use of conventional notations is made throughout, i.e. the stress tensor and the electric displacement field are denoted by $\boldsymbol{\sigma}$ and $\boldsymbol{D}$, whereas $\boldsymbol{n}_{\sigma,D}$ represent unit surface normals, respectively.

The so-called set of nonlinear constitutive equations accounts for the previously mentioned spontaneous polarisation vector $\boldsymbol{P}^{\mathrm{s}} = P^{\mathrm{s}}\,\boldsymbol{m}$ and spontaneous strains $\boldsymbol{\varepsilon}^{\mathrm{s}} = \varepsilon^{\mathrm{s}}\,[\,3\,\boldsymbol{m} \otimes \boldsymbol{m} - \boldsymbol{I}\,]/2$—with the unit-vector $\boldsymbol{m}$ characterising the orientation of the underlying unit-cell—so that

$$\boldsymbol{\sigma} = \mathbf{C} : [\,\boldsymbol{\varepsilon} - \boldsymbol{\varepsilon}^{\mathrm{s}}\,] - \boldsymbol{E} \cdot \boldsymbol{d} \tag{3}$$

$$\boldsymbol{D} = \boldsymbol{d} : [\,\boldsymbol{\varepsilon} - \boldsymbol{\varepsilon}^{\mathrm{s}}\,] + \boldsymbol{\epsilon} \cdot \boldsymbol{E} + \boldsymbol{P}^{\mathrm{s}} \tag{4}$$

with $\boldsymbol{\varepsilon} = \nabla^{\mathrm{sym}}\,\boldsymbol{u}$ and $\boldsymbol{E} = -\nabla\,\phi$ being obvious. Both, the elastic stiffness $\mathbf{C} = \lambda\,\boldsymbol{I} \otimes \boldsymbol{I} + 2\,\mu\,\mathbf{I}^{\mathrm{sym}}$ as well as the dielectric permittivity $\boldsymbol{\epsilon} = \epsilon\,\boldsymbol{I}$ are, for the sake of simplicity, assumed to represent isotropic response (the tensors $\boldsymbol{I}$ and $\mathbf{I}$ denote identity tensors of second and fourth order). The piezoelectric tensor, however, will be enabled to vary from domain to domain as based on a transversely isotropic representation for $\boldsymbol{d}$ such that a tetragonal lattice structure is modelled via

$$\begin{aligned} \boldsymbol{d} = d_{33}\ & \boldsymbol{M} \\ & + d_{31}\big[\,\boldsymbol{m} \otimes \boldsymbol{I} - \boldsymbol{M}\,\big] \\ & + d_{15}\Big[\,\frac{1}{2}\,[\,\boldsymbol{I} \otimes \boldsymbol{m} + \boldsymbol{I} \,\overline{\otimes}\, \boldsymbol{m}\,] - \boldsymbol{M}\,\Big] \end{aligned} \tag{5}$$

with $\boldsymbol{M} = \boldsymbol{m} \otimes \boldsymbol{m} \otimes \boldsymbol{m}$ and $[\,\boldsymbol{I} \otimes \boldsymbol{m} + \boldsymbol{I} \,\overline{\otimes}\, \boldsymbol{m}\,] : \boldsymbol{a} = [\,\boldsymbol{I} \otimes \boldsymbol{m} + \boldsymbol{I} \,\overline{\otimes}\, \boldsymbol{m}\,] : \boldsymbol{a}^{\mathrm{t}}\ \forall\ \boldsymbol{a} \in \mathbb{R}^{3\times3}$. In order to account for an un-poled virgin state within the subsequently elaborated finite element examples, the underlying orientation-vector $\boldsymbol{m}$ will—for each individual finite element—be randomly initiated by means of Eulerian angles from which $\boldsymbol{P}^{\mathrm{s}}|_{t_0}$ and $\boldsymbol{\varepsilon}^{\mathrm{s}}|_{t_0}$ can be computed. For details of implementation and further background information the reader is refer to our previous works, Arockiarajan et al. [12–14].

3 Switching processes

Domain switching effects correspond to a reorientation of the polarisation vector attached to every unit-cell. Referring to a tetragonal microstructure, as elaborated in this contribution, solely 90° or 180° domain switching occurs. Considering a particular time interval $\Delta t = t_{n+1} - t_n > 0$ of interest, switching accordingly transforms the 'initial' polarisation vector either with respect to one out of four possible 90° switching directions or subjected to a 180° switching process.

In the progression of this work, domain switching is initiated by means of an energy criterion. In other words, phase-transformations might occur if the reduction of free energy exceeds a critical threshold. To be specific, the approach advocated by Hwang et al. [8] is adopted, namely

$$\boldsymbol{E} \cdot \Delta \boldsymbol{P}^{\mathrm{s}} + \boldsymbol{\sigma} : \Delta \boldsymbol{\varepsilon}^{\mathrm{s}} > 2\, E_0\, P_0 \tag{6}$$

with $\Delta \boldsymbol{P}^{\mathrm{s}}$, $\Delta \boldsymbol{\varepsilon}^{\mathrm{s}}$ denoting the corresponding change in spontaneous polarisation and strains, whereas $E_0 > 0$ and $P_0 > 0$ characterise the coercive electric field value and the polarisation parameter, respectively. The subsequently studied numerical examples will account for that particular switching state that results in the largest amount of (local) energy reduction.

Furthermore, Eq. 6 can be embedded into both, rate-independent as well as rate-dependent formulations. In view of such time-dependent phase-transformation, a linear kinetics theory is applied in this work; see Delibas et al. [15] and Arockiarajan et al. [14, 16] for detail elaborations. In this regard, a duration time value (Δt_l) is introduced characterising the time interval needed to complete a switching process after its initiation. Here we make use of the ansatz

$$\Delta t_l = \frac{C_1}{\|\boldsymbol{E}\|} + \frac{C_2}{\|\boldsymbol{\sigma}\|} \tag{7}$$

wherein $C_{1,2} > 0$ are temperature- and size-dependent parameters; compare Merz [17].

In view of numerical simulations, the considered time interval between two subsequent loading levels might be smaller than this limit time value ($\Delta t < \Delta t_1$) so that the domain switching process is not completed within that particular load step (Δt). Accordingly, a straightforward volume fraction approach—as reflected by the parameter τ, which represents the fraction between the time elapsed since the switching process has been initiated for a particular loading level and the critical switching (limit) time—is adopted. In this context, this volume fraction is introduced into a modified switching update scheme via

$$\boldsymbol{P}^{\mathrm{s}}_{n+1} = \tau\, \widetilde{\boldsymbol{P}}^{\mathrm{s}}_{n+1} + [\,1 - \tau\,]\, \boldsymbol{P}^{\mathrm{s}}_{n} \tag{8}$$

$$\boldsymbol{\varepsilon}^{\mathrm{s}}_{n+1} = \tau\, \widetilde{\boldsymbol{\varepsilon}}^{\mathrm{s}}_{n+1} + [\,1 - \tau\,]\, \boldsymbol{\varepsilon}^{\mathrm{s}}_{n} \tag{9}$$

wherein $\widetilde{\boldsymbol{P}}^{\mathrm{s}}_{n+1}$, $\widetilde{\boldsymbol{\varepsilon}}^{\mathrm{s}}_{n+1}$ denote the fully switched state while $\boldsymbol{P}^{\mathrm{s}}_{n}$, $\boldsymbol{\varepsilon}^{\mathrm{s}}_{n}$ correspond to the un-switched state.

In general piezoelectric materials exhibit polycrystalline structures such that grains are interconnected with each other at so-called grain boundaries. Accordingly, these boundaries influence the overall response of the entire specimen which is commonly denoted as grain boundary effects and might result in rather large local loading levels. For the sake of simplicity—in other words, to avoid very fine finite element meshes for the numerical examples elaborated later on—such effects are next incorporated via a phenomenologically motivated probability function

$$P = \begin{cases} \left[\dfrac{-\Delta \bar{U}}{2\, E_0\, P_0}\right]^k & \text{for} \quad -\Delta \bar{U} < 2\, E_0\, P_0 \\ 1 & \text{for} \quad -\Delta \bar{U} \geq 2\, E_0\, P_0 \end{cases} \tag{10}$$

wherein $-\Delta \bar{U} = \bar{\boldsymbol{E}}^{\boldsymbol{e}} \cdot \Delta \boldsymbol{P}^{\mathrm{s}\,e} + \bar{\boldsymbol{\sigma}}^{\boldsymbol{e}} : \Delta \boldsymbol{\varepsilon}^{\mathrm{s}\,e}$ and the parameter $k > 0$ enables calibration with experimental measurements. Moreover, volume-averaged quantities with respect to individual domains (one finite element in the following), namely $\bar{\boldsymbol{E}}^{e} = \frac{1}{\mathcal{V}^e} \int_{\mathcal{V}^e} \boldsymbol{E}^{e}\, \mathrm{d}v$ and $\bar{\boldsymbol{\sigma}}^{e} = \frac{1}{\mathcal{V}^e} \int_{\mathcal{V}^e} \boldsymbol{\sigma}^{e}\, \mathrm{d}v$, are considered so that the chosen switching criterion (recall Eq. 6) takes the format

$$\bar{\boldsymbol{E}}^{e} \cdot \Delta \boldsymbol{P}^{\mathrm{s}\,e} + \bar{\boldsymbol{\sigma}}^{e} : \Delta \boldsymbol{\varepsilon}^{\mathrm{s}\,e} > 2\, E_0\, P_0\, P\,. \tag{11}$$

4 Numerical examples

The rate-dependent model discussed above has been implemented within a three-dimensional finite element setting, whereby each crystallite is assumed to be represented by one single (eight-node brick) finite element. Adopting strategies borrowed from computational inelasticity, both, spontaneous polarisation ($\boldsymbol{P}^{\mathrm{s}}$) as well as spontaneous strains ($\boldsymbol{\varepsilon}^{\mathrm{s}}$) are introduced as internal variables stored at the Gauss point level or rather, for the problem at hand, at the element level; see Allik and Hughes [9], Schröder and Gross [5], or Arockiarajan et al. [14, 16] for further background information on algorithmic aspects. As previously mentioned, the orientation of the underlying unit-cells is randomly initialised by means of Eulerian angles. Furthermore, a simple and robust staggered iteration technique is applied to

incorporate switching effects into the developed finite element programme: (a) compute $\boldsymbol{u}$ and ϕ at fixed $\boldsymbol{P}^{\mathrm{s}}$, $\boldsymbol{\varepsilon}^{\mathrm{s}}$ and $\boldsymbol{d}$ for given boundary/loading conditions; (b) compute $\boldsymbol{P}^{\mathrm{s}}$, $\boldsymbol{\varepsilon}^{\mathrm{s}}$ and $\boldsymbol{d}$ based on the switching criterion at fixed $\boldsymbol{u}$ and ϕ; (c) recompute $\boldsymbol{u}$ and ϕ at fixed $\boldsymbol{P}^{\mathrm{s}}$, $\boldsymbol{\varepsilon}^{\mathrm{s}}$ and $\boldsymbol{d}$ for identical boundary/loading conditions. Please note that all finite elements are allowed to switch at the same time. In the following, we address the simulation of a block-like specimen under different loading conditions, see also Fig. 1:

(i, Section 4.1) Electrical loading is applied by means of prescribing the electric potential at the top surface—, ϕ^{p}_{top}, and bottom surface, ϕ^{p}_{bot}. The electric potential is zero at the bottom nodes while the electric potential on the top nodes is (quasi-statically) incrementally increased and decreased in a cyclic manner. Otherwise, charge-free conditions are chosen.

(ii, Section 4.2) Mechanical loading is applied by means of prescribing traction at the top surface, $\boldsymbol{t}^{p}_{\mathrm{top}}$, and displacements at the bottom surface, $\boldsymbol{u}^{p}_{\mathrm{bot}}$. The displacements are zero at the bottom nodes while the traction on the top-nodes is (quasi-statically) incrementally increased and decreased in a cyclic manner. Otherwise, traction-free conditions are chosen.

In view of investigating macroscopic properties of a bulk ceramic specimen, simple volume-averaging techniques are applied to the obtained three-dimensional finite element results such that, by making use of an additional projection onto the loading direction $\boldsymbol{e}_3$, representative hysteresis and butterfly loops as well as stress versus strain curves can be computed, to be specific

$$\mathsf{D} = \frac{1}{\mathcal{V}^{B}} \int_{\mathcal{B}} \boldsymbol{e}_3 \cdot \boldsymbol{D} \; \mathrm{d}v \,,$$

$$\mathsf{E} = \frac{1}{\mathcal{V}^{B}} \int_{\mathcal{B}} \boldsymbol{e}_3 \cdot \boldsymbol{E} \; \mathrm{d}v \,,$$

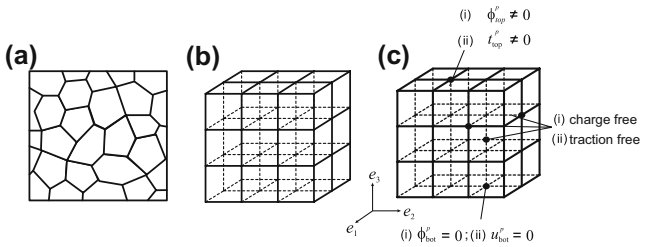

Fig. 1 (**a**) assembly of grains—two-dimensional illustration, (**b**) sketch of a finite element mesh—three-dimensional discretisation, and (**c**) boundary conditions applied to the specimen

$$\mathsf{e} = \frac{1}{\mathcal{V}^{B}} \int_{\mathcal{B}} \boldsymbol{e}_3 \cdot \boldsymbol{\varepsilon} \cdot \boldsymbol{e}_3 \; \mathrm{d}v \,,$$

$$\mathsf{s} = \frac{1}{\mathcal{V}^{B}} \int_{\mathcal{B}} \boldsymbol{e}_3 \cdot \boldsymbol{\sigma} \cdot \boldsymbol{e}_3 \; \mathrm{d}v \,. \tag{12}$$

Within the following finite element simulations a block-like specimen, namely a $9 \times 9 \times 9$ cube, is approximated by a discretisation with $9 \times 9 \times 9$ linear eight node bricks (Q1Q1)—the edges of the mesh being aligned with the global Cartesian frame $\{\boldsymbol{e}_{1,2,3}\}$; compare Fig. 1. Furthermore, PIC 151 material parameters are adopted from the literature, compare Lu et al. [6]: $\epsilon = 0.0666$ $[\mu\, F/m]$, $d_{33} = 1.52 \times 10^{-9}$ $[m/V]$, $d_{31} = -0.57 \times 10^{-9}$ [m/V], $d_{15} = 1.856 \times 10^{-9}$ [m/V], Young's modulus $E = \mu\,[3\lambda + 2\mu]/[\lambda + \mu] = 30.3$ [GPa], Poisson ratio $\nu = \lambda/[2\lambda + 2\mu] = 0.3$, $\varepsilon^{\mathrm{s}} = 2.7 \times 10^{-3}$, $P^{\mathrm{s}} = P_0 = 0.1938$ [C/m^2], $E_0 = 0.4$ [MV/m], $\sigma_0 = 25$ [MPa] and, moreover, $C_1 = 0.00325$ [MV s/m], $C_2 = 0.00325$ [MPa s] as well as $|\Delta\phi^{p}_{\mathrm{top}}| = 1.0$ [KV], $|\Delta t^{p}_{\mathrm{top}}| = 50$ [KN].

4.1 Ferroelectric switching

Figures 2, 3 and 4 show hysteresis and butterfly loops for various loading amplitudes ($\widehat{\mathsf{E}} = 2.0$ [MV/m], $\widehat{\mathsf{E}} = 1.5$ [MV/m], and $\widehat{\mathsf{E}} = 1.0$ [MV/m]) and frequencies ($f_\phi = 0.05$ [Hz], $f_\phi = 0.50$ [Hz], and $f_\phi = 5.00$ [Hz]), whereby the modelling of intergranular effects is incorporated via Eq. 10 with $k = 5$. As discussed in Section 3, the beginning of the nucleation of the new phases is identified by making use of the energy criterion in Eq. 6 or rather Eq. 11. It is, however, experimentally observed that the coercive electric field depends on the loading frequency as monitored by the rate-dependent numerical results in Figs. 2, 3 and 4 which are based on the ansatz highlighted in Eqs. 8, 9. As a result, we observe that the coercive electric field increases at higher loading frequencies irrespective of the particular loading amplitudes. Another meaningful result is that the electric displacements and longitudinal strain may increase upon reverse loading at higher loading frequencies—even if the value of the electric field decreases. The results shown in Figs. 2 and 3 take the interpretation as the evolution of both, the electric displacements as well as of strains not being saturated for $f_\phi = 5.00$ [Hz] as compared with an almost quasi-static loading at $f_\phi = 0.05$ [Hz] or $f_\phi = 0.50$ [Hz]. Rather both, the electric displacement and strain contribution increases for a decreasing electric field upon reverse loading (for $f_\phi = 5.00$ [Hz]) until the electric field turns out to become smaller than the coercive electric field

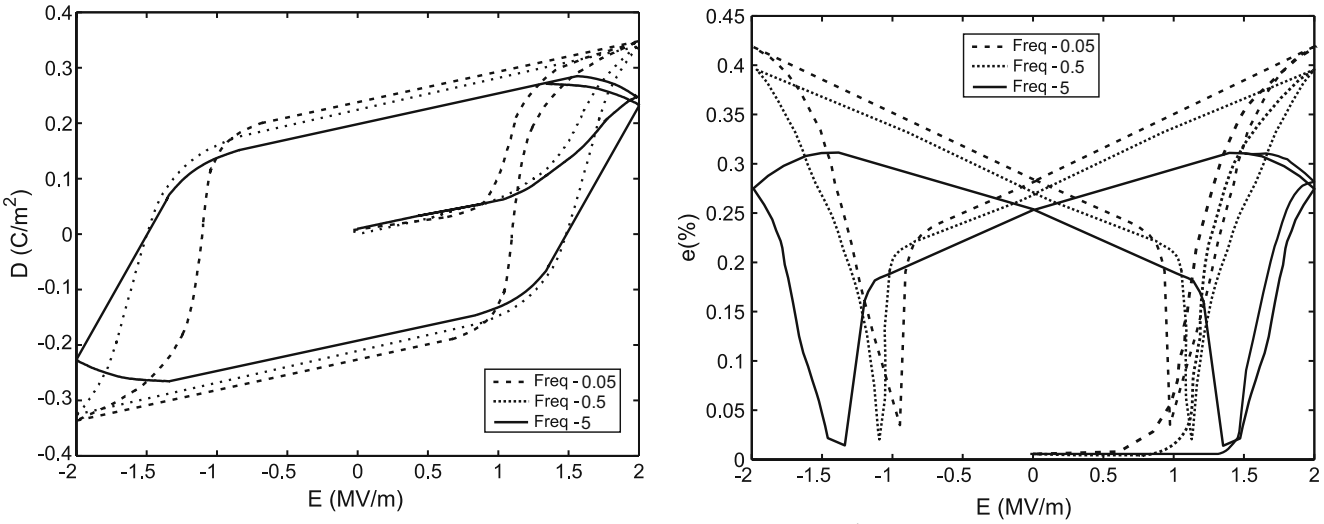

Fig. 2 Hysteresis and butterfly curves with fifth order probability function ($k = 5$) for $\widehat{\mathrm{E}} = 2.0$ [MV/m]

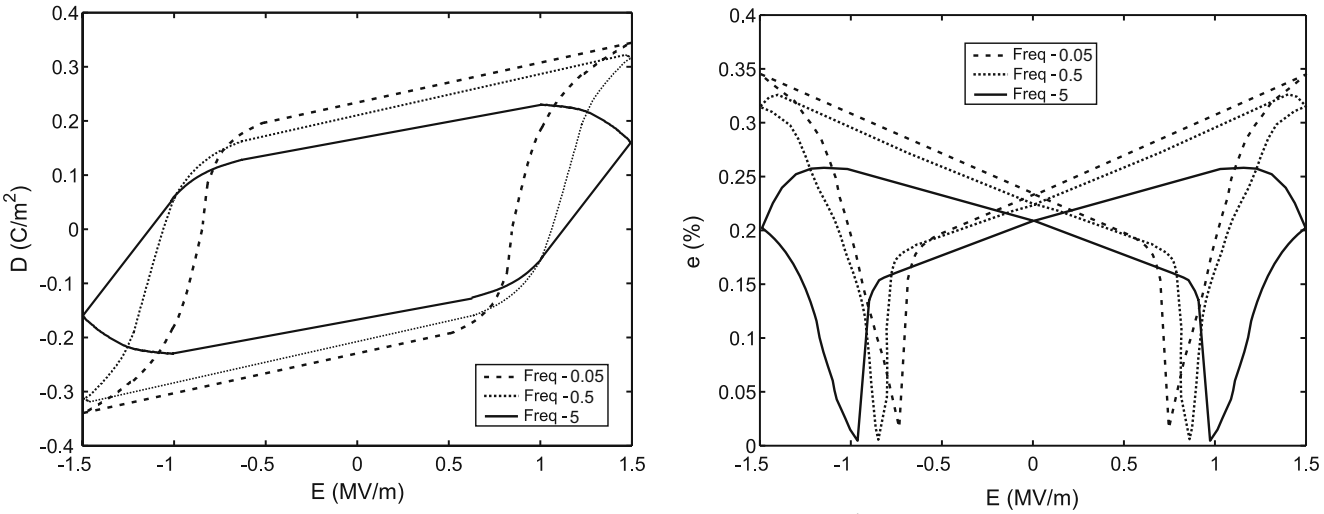

Fig. 3 Hysteresis and butterfly curves with fifth order probability function ($k = 5$) for $\widehat{\mathrm{E}} = 1.5$ [MV/m]

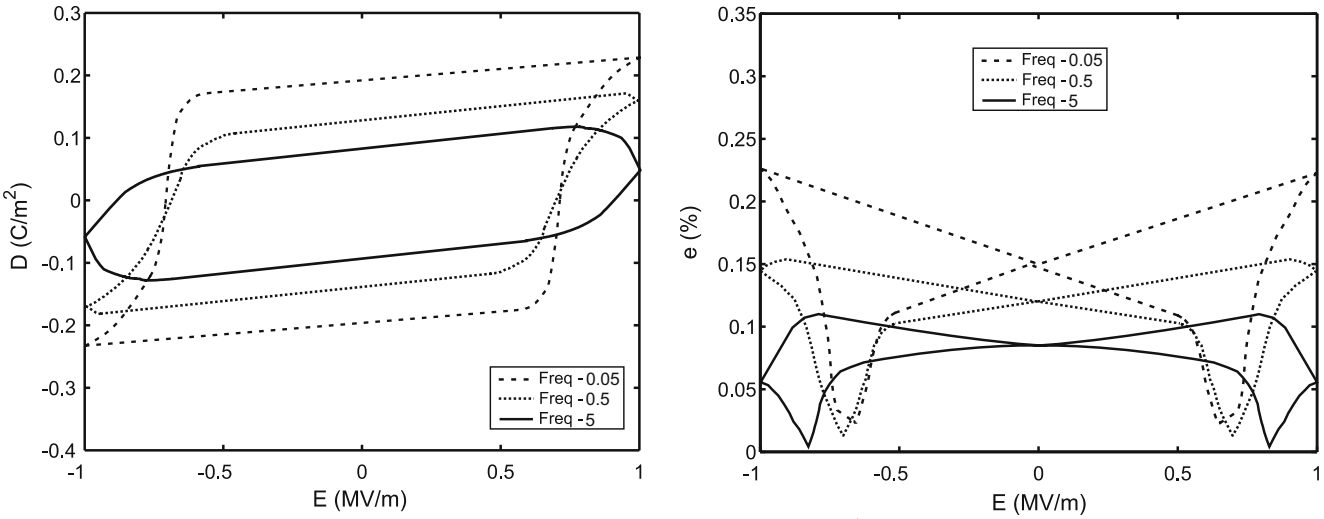

Fig. 4 Hysteresis and butterfly curves with fifth order probability function ($k = 5$) for $\widehat{\mathrm{E}} = 1.0$ [MV/m]

value. Moreover, Figs. 2 and 3 underpin that the remanent polarisation value (in other words the electrical displacement at zero electric field) and remanent strain level (in other words the longitudinal strain at zero electric field) are not shifting significantly when varying the loading frequency ($f_\phi = 0.05$ [Hz] and $f_\phi = 0.50$ [Hz]) for the electric field amplitudes $\widehat{\mathrm{E}} = 2.0$ [MV/m] and $\widehat{\mathrm{E}} = 1.5$ [MV/m], respectively. Apparently, this effect results from possible domain switchings being more or less completed after one simulation step. It is, however, reflected by Fig. 4 that the remanent polarisation value as well as the remanent strain level may significantly decrease with increasing loading frequencies.

4.2 Ferroelastic switching

Figures 5, 6 and 7 show stress versus strain curves for various loading amplitudes ($\widehat{\sigma} = 100$ [MPa], $\widehat{\sigma} = 75$ [MPa], and $\widehat{\sigma} = 50$ [MPa]) and frequencies ($f_t = 0.01$ [Hz], $f_t = 0.10$ [Hz], and $f_t = 1.00$ [Hz]), whereby the switching criterion has been modified as $\bar{\boldsymbol{\sigma}}^e : \Delta\boldsymbol{\varepsilon}^{s\,e} > \frac{3}{2}\sigma_0\varepsilon_0\, P$ with $\varepsilon_0 = \varepsilon^s$, compare Eq. 11, and the probability function is defined via $P = \big[-\Delta\bar{U}/\big[\frac{3}{2}\,\sigma_0\,\varepsilon_0\,\big]\big]^k$ for $-\Delta\bar{U} < \frac{3}{2}\,\sigma_0\,\varepsilon_0$ while $P = 1$ for $-\Delta\bar{U} \geq \frac{3}{2}\,\sigma_0\,\varepsilon_0$, wherein $-\Delta\bar{U} = \bar{\boldsymbol{\sigma}}^e : \Delta\boldsymbol{\varepsilon}^{s\,e}$; compare Eq. 10. It is, however, experimentally observed that the coercive stress level depends on the loading frequency as monitored by the rate-dependent numerical results in Figs. 5, 6 and 7. As a result, we observe that the coercive stress value increases at higher loading frequencies irrespective of the particular loading amplitudes. Another meaningful result is that the longitudinal strains may increase upon reverse loading at higher loading frequencies—even if the value of the stresses decreases. The results shown in Figs. 5 and 6 take the interpretation as the evolution of strains not being saturated for $f_t = 1.00$ [Hz] as compared with an almost quasi-static loading at $f_t = 0.10$ [Hz] or $f_t = 0.01$ [Hz]. Rather, the strain contribution increases for a decreasing tensile stress upon reverse loading (for $f_t = 1.00$ [Hz]) until the stresses turn out to become smaller than the coercive stress value. Moreover, Figs. 5 and 6 underpin that the remanent strain value (in other words the longitudinal strain at zero stresses) is not shifting significantly when varying the loading frequency ($f_t = 0.01$ [Hz] and $f_t = 0.10$ [Hz]) for the traction amplitudes $\widehat{\sigma} = 100$ [MPa] and $\widehat{\sigma} = 75$ [MPa], respectively. Apparently, this effect results from possible domain switchings being more or less completed after one simulation step. It is, however, reflected by Fig. 7 that the remanent strain level may decreases with increasing loading frequencies.

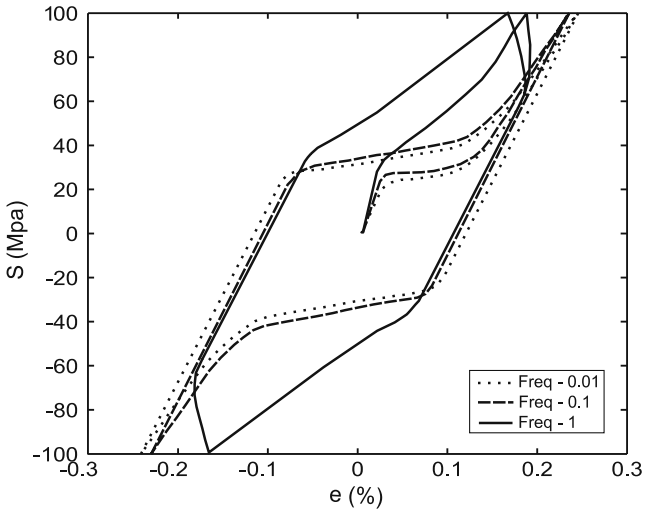

Fig. 5 Stress versus strain curve with fifth order probability function ($k = 5$) for $\widehat{\sigma} = 100$ [MPa]

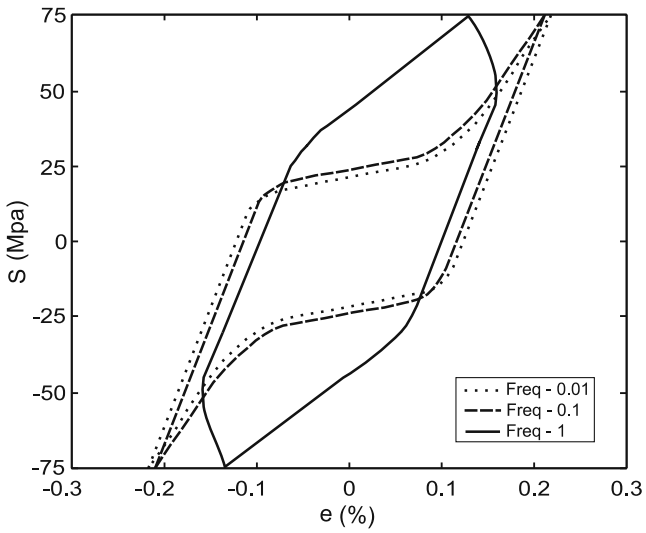

Fig. 6 Stress versus strain curve with fifth order probability function ($k = 5$) for $\widehat{\sigma} = 75$ [MPa]

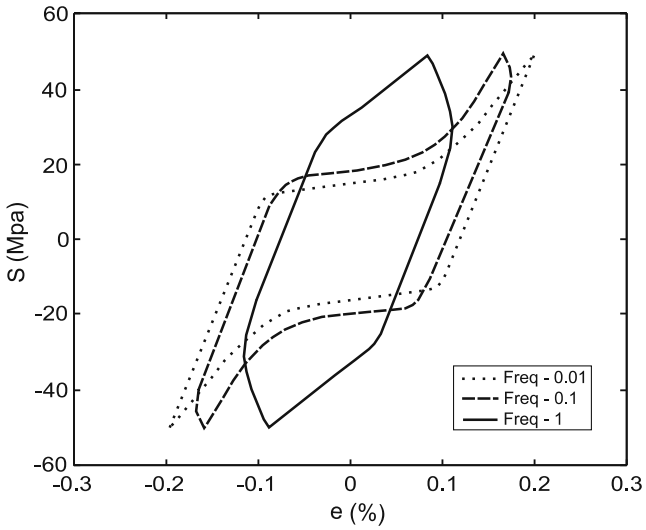

Fig. 7 Stress versus strain curve with fifth order probability function ($k = 5$) for $\widehat{\sigma} = 50$ [MPa]

5 Summary

The nonlinear behaviour of poly-crystalline ferroelectric and ferroelastic materials has been modelled by making use of a micro-mechanically motivated approach, whereby an energy-based switching criterion served for triggering the onset of domain switching. To capture experimentally observed rate-dependent effects, volume fraction concepts were adopted and combined with a linear kinetics theory. Furthermore, the simulation of so-called grain boundary effects was introduced by means of a phenomenological probabilistic approach which conveniently enabled, together with straightforward volume averaging techniques, realistic three-dimensional simulations as based on a coupled finite element formulation. To highlight the overall macroscopic response of representative piezoelectric ceramics, electric field versus electric displacement—electric field versus strains—strains versus stresses curves have been computed for various loading frequencies and amplitudes. Accordingly, the obtained numerical results provide further insight into the general behaviour of ferroelectric and ferroelastic ceramics. At this stage however, related representative experimental data is not accessible to the authors so that detailed comparisons of the highlighted simulation results with meaningful measurements remains to be elaborated. In future, robust modelling approaches capturing switching effects, as the one presented in this contribution, will enable to extend simulations of smart structures with sensors and in particular actuators functioning until now in the linear regime to large loading levels. Naming solely few examples of already established innovative manufacturing techniques, consider for instance rapid prototyping and stereolithography, which serves to 'print' layers of ferroelectric and layers of metal electrode material to produce complex structures in the green state that, later on, can be co-fired; see, among others, e.g. Landis [18] in this regard. Such new technologies are applied to produce rather complex ferroelectric ceramic metal electrode structures and thereby enhance the development of a broad range of novel ferroelectric-materials-based actuators at low costs.

References

1. B. Jaffe, W.R. Cook, H. Jaffe, *Piezoelectric Ceramics* (Academic, London, New York, 1971)
2. C.S. Lynch, R.M. McMeeking, Ferroelectrics **160**, 177 (1994)
3. M. Kamlah, C. Tsakmakis, Int. J. Solids Struct. **36**, 669 (1999)
4. C.M. Landis, J. Mech. Phys. Solids **50**, 127 (2002)
5. J. Schröder, D. Gross, Arch. Appl. Mech. **73**, 533 (2004)
6. W. Lu, D.-N. Fang, C.Q. Li, K.C. Hwang, Acta Mater. **47**, 2913 (1999)
7. X. Chen, D.N. Fang, K.C. Hwang, Acta Mater. **45**, 3189 (1997)
8. S.C. Hwang, C.S. Lynch, R.M. McMeeking, Acta Metall. Mater. **5**, 2073 (1995)
9. H. Allik, T.J.R. Hughes, Int. J. Numer. Methods Eng. **2**, 151 (1970)
10. P. Gaudenzi, K.J. Bathe, J. Intell. Mater. Syst. Struct. **6**, 266 (1995)
11. S.C. Hwang, R. Waser, Acta Mater. **48**, 3271 (2000)
12. A. Arockiarajan, A. Menzel, B. Delibas, W. Seemann, J. Intell. Mater. Syst. Struct. (2006) (in press)
13. A. Arockiarajan, B. Delibas, A. Menzel, W. Seemann, Comput. Mater. Sci. **37**, 306 (2006)
14. A. Arockiarajan, A. Menzel, B. Delibas, W. Seemann, Eur. J. Mech. A, Solids **25**, 950 (2006)
15. B. Delibas, A. Arockiarajan, W. Seemann, Int. J. Solids Struct. **43**, 697 (2006)
16. A. Arockiarajan, A. Menzel, Comput. Model. Eng. Sci. **626**, 1 (2008)
17. W.J. Merz, Phys. Rev. **95**, 690 (1954)
18. C.M. Landis, Curr. Opin. Solid State Mater. Sci. **8**, 59 (2004)